Electronic Supplementary Material (ESI) for Nanoscale.

Supplementary materials for

Solar cells based on 2D Janus group-III chalcogenide van der Waals heterostructures

M. Bikerouin*, O. Chdil, M. Balli**

AMEEC team, LERMA, College of Engineering and Architecture, International University of Rabat, parc Technopolis, Rocade de Rabat-Salé, 11100, Morocco.

*Email: mouad.bikerouin@uir.ac.ma

**Email: mohamed.balli@uir.ac.ma

Text S1. Formalism for the calculation of the mechanical properties

- The Young modulus:

$$\Upsilon = \frac{C_{11}^2 - C_{12}^2}{C_{11}} \quad (1)$$

- The Poisson ratio:

$$\nu = \frac{C_{12}}{C_{11}} \quad (2)$$

- The 2D layer modulus:

$$\gamma^{2D} = \frac{C_{11} + C_{12}}{2} \quad (3)$$

- The intrinsic strength:

$$\sigma_{int} \simeq \frac{\Upsilon}{9} \quad (4)$$

- The bending modulus:

$$\mathrm{D} = \frac{\Upsilon\, h^2}{12(1-\nu^2)} \quad (5)$$

where h is the nanosheet thickness.

Text S2. Formalism for the calculation of the cohesive energy and the heat of formation

Cohesive energy (E_{coh}) of MM'XY monolayer is calculated using the following formula [1],

$$E_c = \frac{N_M E_M^{iso} + N_{M'} E_{M'}^{iso} + N_X E_X^{iso} + N_Y E_Y^{iso} - E_{MM'XY}}{N_M + N_{M'} + N_X + N_Y}, \quad (6)$$

where $E_{MM'XY}$ refers to the total energy of the MM'XY monolayer, E_M^{iso}, $E_{M'}^{iso}$, E_X^{iso}, and E_Y^{iso} represent the single atom energies of M, M', X, and Y elements, respectively, and N_M, $N_{M'}$, N_X, and N_Y stand for the number of corresponding elements in the unit cell.

The heat of formation (ΔH) of MM'XY monolayer is determined using the following equation [2],

$$\Delta H = \frac{E_{MM'XY} - n_M E_M^{SS} - n_{M'} E_{M'}^{SS} - n_X E_X^{SS} - n_Y E_Y^{SS}}{n}, \quad (7)$$

where $E_{MM'XY}$ is to the total energy of the MM'XY monolayer, E_M^{SS}, $E_{M'}^{SS}$, E_X^{SS}, and E_Y^{SS} are the energies of the M, M', X, and Y atoms in their solid phase, respectively; n_M, $n_{M'}$, n_X, and n_Y represent the numbers of atoms for each element in the unit cell of MM'XY, and n is the total number of atoms in the unit cell.

Table S1. Calculated lattice parameter (a), bond lengths ($d_{\mathrm{M-X}}$, $d_{\mathrm{M'-Y}}$, and $d_{\mathrm{M-M'}}$), thickness (h), band gaps using HSE (E_g^{HSE}) and HSE+SOC ($E_g^{HSE+SOC}$) exchange-correlation potentials, potential energy difference ($\Delta\phi$), and dipole moment (P) of MX, M_2XY, $MM'X_2$, and MM'XY (M, M' = Ga, In; X, Y = S, Se, Te) monolayers.

Type	Materials	a (Å)	$d_{\mathrm{M-X}}$ (Å)	$d_{\mathrm{M'-Y}}$ (Å)	$d_{\mathrm{M-M'}}$ (Å)	h (Å)	E_g^{HSE} (eV)	$E_g^{HSE+SOC}$ (eV)	$\Delta\phi$ (eV)	P (Debye)
MX	GaS	3.57	2.34	2.34	2.44	4.64	3.47	3.47	0	0
	GaSe	3.74	2.47	2.47	2.43	4.82	3.12	3.08	0	0
	GaTe	4.05	2.67	2.67	2.43	5.01	2.34	2.02	0	0
	InS	3.79	2.52	2.52	2.79	5.28	3.07	3.07	0	0
	InSe	3.93	2.64	2.64	2.78	5.48	2.81	2.70	0	0
	InTe	4.23	2.84	2.84	2.78	5.69	2.35	1.99	0	0
M_2XY	Ga_2SSe	3.66	2.36	2.44	2.43	4.73	3.29	3.12	0.25	0.07
	Ga_2STe	3.83	2.42	2.61	2.43	4.80	1.59	1.26	0.57	0.19
	Ga_2SeTe	3.91	2.52	2.63	2.43	4.91	2.01	1.69	0.34	0.12
	In_2SSe	3.86	2.53	2.63	2.79	5.38	2.69	2.53	0.22	0.08
	In_2STe	4.02	2.57	2.80	2.79	5.47	1.41	1.09	0.48	0.18
	In_2SeTe	4.09	2.68	2.81	2.78	5.58	1.81	1.48	0.28	0.11
$MM'X_2$	$GaInS_2$	3.68	2.37	2.49	2.61	4.98	3.13	3.12	0.40	0.12
	$GaInSe_2$	3.82	2.49	2.62	2.61	5.17	2.52	2.35	0.27	0.09
	$GaInTe_2$	4.13	2.70	2.82	2.60	5.37	1.97	1.61	0.15	0.06
MM'XY	GaInSSe	3.74	2.39	2.60	2.61	5.09	2.13	1.96	0.08	0.03
	GaInSTe	3.90	2.44	2.78	2.61	5.20	0.53	0.22	0.36	0.13
	GaInSeTe	3.98	2.54	2.79	2.61	5.29	1.02	0.70	0.16	0.05
	InGaSSe	3.76	2.51	2.48	2.61	5.06	3.04	3.01	0.56	0.18
	InGaSTe	3.94	2.55	2.64	2.61	5.11	2.31	1.99	0.73	0.26
	InGaSeTe	4.00	2.65	2.66	2.61	5.24	2.57	2.23	0.50	0.18

Table S2. Calculated cohesive energy (E_{coh}), heat of formation (ΔH), and energy above the convex hull (ΔH_{hull}), as well as the thermodynamic stability indicator of MX, M_2XY, $MM'X_2$, and MM'XY (M, M' = Ga, In; X, Y = S, Se, Te) monolayers. The thermodynamic stability criterion is defined as follows [3]: low ($\Delta H > 0.2$ eV/atom), medium ($\Delta H < 0.2$ eV/atom and $\Delta H_{hull} > 0.2$ eV/atom), and high ($\Delta H < 0.2$ eV/atom and $\Delta H_{hull} < 0.2$ eV/atom).

Type	Materials	E_{coh} (eV/atom)	ΔH (eV/atom)	ΔH_{hull} (eV/atom)	Thermodynamic stability
MX	GaS	3.61	-0.66	0.01	High
	GaSe	3.32	-0.59	0.01	High
	GaTe	2.95	-0.35	0.01	High
	InS	3.31	-0.52	0.01	High
	InSe	3.07	-0.50	0.03	High
	InTe	2.76	-0.32	0.02	High
M_2XY	Ga_2SSe	3.46	-0.61	0.01	High
	Ga_2STe	3.21	-0.44	0.07	High
	Ga_2SeTe	3.11	-0.44	0.03	High
	In_2SSe	3.18	-0.50	0.03	High
	In_2STe	2.99	-0.38	0.06	High
	In_2SeTe	2.90	-0.40	0.04	High
$MM'X_2$	$GaInS_2$	3.43	-0.56	0.04	High
	$GaInSe_2$	3.17	-0.52	0.04	High
	$GaInTe_2$	2.83	-0.32	0.04	High
MM'XY	GaInSSe	3.28	-0.51	0.08	High
	GaInSTe	3.04	-0.34	0.16	High
	GaInSeTe	2.96	-0.37	0.10	High
	InGaSSe	3.30	-0.54	0.05	High
	InGaSTe	3.12	-0.42	0.08	High
	InGaSeTe	3.01	-0.42	0.05	High

Table S3. Bader charges (in *e*) of all elements constituting the studied group-III chalcogenides monolayers. Positive Bader charges represent charge accumulation, whereas negative values represent charge depletion.

MX										
GaS		GaSe		GaTe		InS		InSe		InTe	
S	0.840	Se	0.681	Te	0.453	S	0.836	Se	0.702	Te	0.517
Ga	-0.855	Ga	-0.696	Ga	-0.469	In	-0.849	In	-0.715	In	-0.530
Ga	-0.825	Ga	-0.666	Ga	-0.437	In	-0.823	In	-0.689	In	-0.504
S	0.840	Se	0.681	Te	0.453	S	0.836	Se	0.702	Te	0.517
M_2XY										
Ga_2SSe		Ga_2STe		Ga_2SeTe		In_2SSe		In_2STe		In_2SeTe	
S	0.841	S	0.842	Se	0.683	S	0.842	S	0.855	Se	0.712
Ga	-0.837	Ga	-0.853	Ga	-0.687	In	-0.861	In	-0.882	In	-0.710
Ga	-0.684	Ga	-0.434	Ga	-0.444	In	-0.677	In	-0.476	In	-0.509
Se	0.680	Te	0.445	Te	0.448	Se	0.696	Te	0.503	Te	0.507
$MM'X_2$										
$GaInS_2$				$GaInSe_2$				$GaInTe_2$			
S	0.839			Se	0.680			Te	0.455		
Ga	-0.809			Ga	-0.649			Ga	-0.421		
In	-0.855			In	-0.726			In	-0.545		
S	0.825			Se	0.695			Te	0.511		
MM'XY										
GaInSSe		GaInSTe		GaInSeTe		InGaSSe		InGaSTe		InGaSeTe	
S	0.838	S	0.838	Se	0.681	S	0.834	S	0.850	Se	0.708
Ga	-0.816	Ga	-0.822	Ga	-0.650	In	-0.873	In	-0.903	In	-0.756
In	-0.709	In	-0.509	In	-0.532	Ga	-0.640	Ga	-0.394	Ga	-0.402
Se	0.687	Te	0.493	Te	0.501	Se	0.679	Te	0.447	Te	0.450

Table S4. Calculated elastic constants (C_{11}, C_{12}, and C_{66}), Young modulus (ϒ), Poisson ratio (ν), layer modulus (γ^{2D}), intrinsic strength (σ_{int}), and bending modulus (D) of MX, M_2XY, $MM'X_2$, and MM'XY (M, M' = Ga, In; X, Y = S, Se, Te) monolayers.

Type	Materials	C_{11} (N m^{-1})	C_{12} (N m^{-1})	C_{66} (N m^{-1})	ϒ (N m^{-1})	ν	γ^{2D} (N m^{-1})	σ_{int} (N m^{-1})	D (eV)
MX	GaS	99	25	37	93	0.25	62	10	11
	GaSe	83	20	31	78	0.25	51	9	10
	GaTe	66	16	25	63	0.23	41	7	9
	InS	67	20	23	61	0.30	43	7	10
	InSe	55	16	20	51	0.29	36	6	9
	InTe	44	12	16	41	0.26	28	5	8
M_2XY	Ga_2SSe	89	22	34	84	0.25	56	9	10
	Ga_2STe	72	17	28	68	0.23	44	8	9
	Ga_2SeTe	71	17	27	67	0.23	44	7	9
	In_2SSe	61	18	21	55	0.30	39	6	9
	In_2STe	53	14	20	49	0.27	34	6	8
	In_2SeTe	49	13	18	46	0.27	31	5	8
$MM'X_2$	$GaInS_2$	82	23	30	76	0.28	53	8	11
	$GaInSe_2$	69	19	25	64	0.27	44	7	10
	$GaInTe_2$	55	14	20	51	0.25	34	6	8
MM'XY	GaInSSe	74	21	27	69	0.28	48	8	10
	GaInSTe	62	16	23	58	0.25	39	6	9
	GaInSeTe	58	15	22	54	0.26	37	6	8
	InGaSSe	75	20	27	69	0.27	48	8	10
	InGaSTe	65	16	24	61	0.25	41	7	9
	InGaSeTe	61	16	23	57	0.26	38	6	9

Table S5. Calculated carrier effective mass (m^*), deformation potential constant (E_l), and carrier mobility (μ) for electron (e) and hole (h) along the zigzag (x) and armchair (y) directions at 300 K in single-layers MX, M_2XY, and $MM'X_2$ (M, M' = Ga, In; X, Y = S, Se, Te).

Type	Materials	Carrier type	m_x^* (m_0)	m_y^* (m_0)	E_{lx} (eV)	E_{ly} (eV)	μ_x ($cm^2\ V^{-1}\ s^{-1}$)	μ_y ($cm^2\ V^{-1}\ s^{-1}$)
MX	GaS	Electron	0.92	0.32	6.06	2.22	115.01	2463.94
		Hole	1.78	1.29	2.63	3.00	113.01	119.84
	GaSe	Electron	0.37	0.21	9.03	7.90	210.19	483.85
		Hole	1.30	1.13	2.24	2.64	223.59	185.18
	GaTe	Electron	0.26	0.22	5.97	2.59	634.22	3982.38
		Hole	1.33	1.17	3.19	2.96	83.26	109.92
	InS	Electron	0.33	0.18	4.43	4.44	904.02	1649.92
		Hole	2.30	1.23	3.02	3.31	40.44	62.95
	InSe	Electron	0.26	0.18	5.13	5.13	791.32	1143.01
		Hole	1.60	1.05	1.81	1.57	172.40	349.17
	InTe	Electron	0.35	0.22	3.78	1.73	675.27	5128.75
		Hole	0.79	0.70	5.53	5.36	52.16	62.66
M_2XY	Ga_2SSe	Electron	0.36	0.21	8.55	3.58	261.95	2561.31
		Hole	0.89	0.79	4.84	4.53	108.42	139.44
	Ga_2STe	Electron	0.26	0.21	6.02	6.03	696.45	859.41
		Hole	0.53	0.24	8.62	8.35	109.17	256.94
	Ga_2SeTe	Electron	0.18	0.12	7.25	6.62	1087.43	1956.38
		Hole	0.57	0.28	7.84	7.60	108.03	234.03
	In_2SSe	Electron	0.30	0.17	4.73	4.74	857.08	1506.11
		Hole	0.95	0.60	5.34	5.17	63.52	107.29
	In_2STe	Electron	0.29	0.16	4.50	4.50	892.30	1617.30
		Hole	0.65	0.28	7.12	6.91	80.29	197.90
	In_2SeTe	Electron	0.25	0.18	5.32	5.33	695.26	962.01
		Hole	0.68	0.30	6.75	6.55	74.57	179.51
$MM'X_2$	$GaInS_2$	Electron	0.31	0.28	6.93	6.55	398.15	493.44
		Hole	1.32	1.15	2.61	2.36	157.63	221.30
	$GaInSe_2$	Electron	0.24	0.22	7.16	7.18	519.77	563.87
		Hole	0.94	0.49	6.50	6.32	54.52	110.63
	$GaInTe_2$	Electron	0.32	0.27	5.28	2.27	446.69	2864.24
		Hole	0.71	0.34	6.72	6.63	74.36	159.52

Table S6. Calculated carrier effective mass (m^*), deformation potential constant (E_l), and carrier mobility (μ) for electron (e) and hole (h) along the zigzag (x) and armchair (y) directions at 300 K in single-layers MM'XY (M, M' = Ga, In; X, Y = S, Se, Te).

Type	Materials	Carrier type	m_x^* (m_0)	m_y^* (m_0)	E_{lx} (eV)	E_{ly} (eV)	μ_x ($cm^2\ V^{-1}\ s^{-1}$)	μ_y ($cm^2\ V^{-1}\ s^{-1}$)
MM'XY	GaInSSe	Electron	0.27	0.21	6.72	6.73	542.82	695.84
		Hole	0.91	0.37	7.23	7.03	57.10	148.53
	GaInSTe	Electron	0.32	0.15	7.12	7.04	371.52	810.69
		Hole	0.61	0.26	7.76	7.21	90.26	245.31
	GaInSeTe	Electron	0.21	0.15	5.81	5.82	981.79	1369.79
		Hole	0.64	0.28	8.35	8.12	65.39	158.05
	InGaSSe	Electron	0.33	0.24	7.07	7.08	344.08	471.78
		Hole	1.68	1.08	2.64	3.02	101.27	120.39
	InGaSTe	Electron	0.49	0.28	6.10	5.45	204.97	449.37
		Hole	0.58	0.32	6.62	6.38	126.41	246.69
	InGaSeTe	Electron	0.59	0.30	5.67	2.10	162.80	2334.00
		Hole	0.82	0.75	6.18	5.98	52.90	61.77

Table S7. Calculated lattice parameter (a), interlayer distance (d), thickness (h), binding energy (E_b), bandgap using HSE functional (E_g^{HSE}), potential energy difference ($\Delta\phi$), and dipole moment (P) of different stacking configurations of $Ga_2STe/GaInS_2$ van der Waals (vdW) heterostructure.

Stacking	Patterns	a (Å)	d (Å)	h (Å)	E_b (eV)	E_g^{HSE} (eV)	$\Delta\phi$ (eV)	P (Debye)
AA	P1	3.75	3.74	13.52	-0.099	0.98	0.29	0.09
	P2	3.75	3.82	13.60	-0.089	1.25	0.87	0.28
	P3	3.75	3.85	13.63	-0.137	0.54	0.68	0.22
	P4	3.75	3.91	13.70	-0.123	0.81	0.21	0.07
AB	P1	3.76	3.01	12.77	-0.165	0.97	0.28	0.09
	P2	3.76	3.05	12.81	-0.154	1.27	0.88	0.28
	P3	3.76	3.16	12.93	-0.225	0.64	0.64	0.21
	P4	3.76	3.21	12.98	-0.205	0.91	0.14	0.05
AC	P1	3.75	3.74	13.53	-0.100	0.98	0.29	0.09
	P2	3.75	3.82	13.60	-0.089	1.25	0.87	0.28
	P3	3.75	3.84	13.63	-0.138	0.54	0.68	0.22
	P4	3.75	3.91	13.69	-0.123	0.81	0.21	0.07
AD	P1	3.76	3.00	12.75	-0.163	0.97	0.27	0.09
	P2	3.76	3.02	12.78	-0.154	1.24	0.87	0.28
	P3	3.76	3.15	12.92	-0.223	0.66	0.63	0.20
	P4	3.76	3.18	12.95	-0.207	0.94	0.11	0.04
AE	P1	3.76	2.96	12.72	-0.162	0.98	0.28	0.09
	P2	3.76	2.98	12.74	-0.153	1.23	0.87	0.28
	P3	3.76	3.17	12.94	-0.215	0.65	0.63	0.21
	P4	3.76	3.20	12.97	-0.199	0.92	0.12	0.04
AF	P1	3.76	2.97	12.72	-0.167	0.99	0.28	0.09
	P2	3.76	3.01	12.77	-0.155	1.27	0.89	0.29
	P3	3.76	3.17	12.94	-0.221	0.64	0.64	0.21
	P4	3.76	3.22	12.99	-0.201	0.90	0.15	0.05

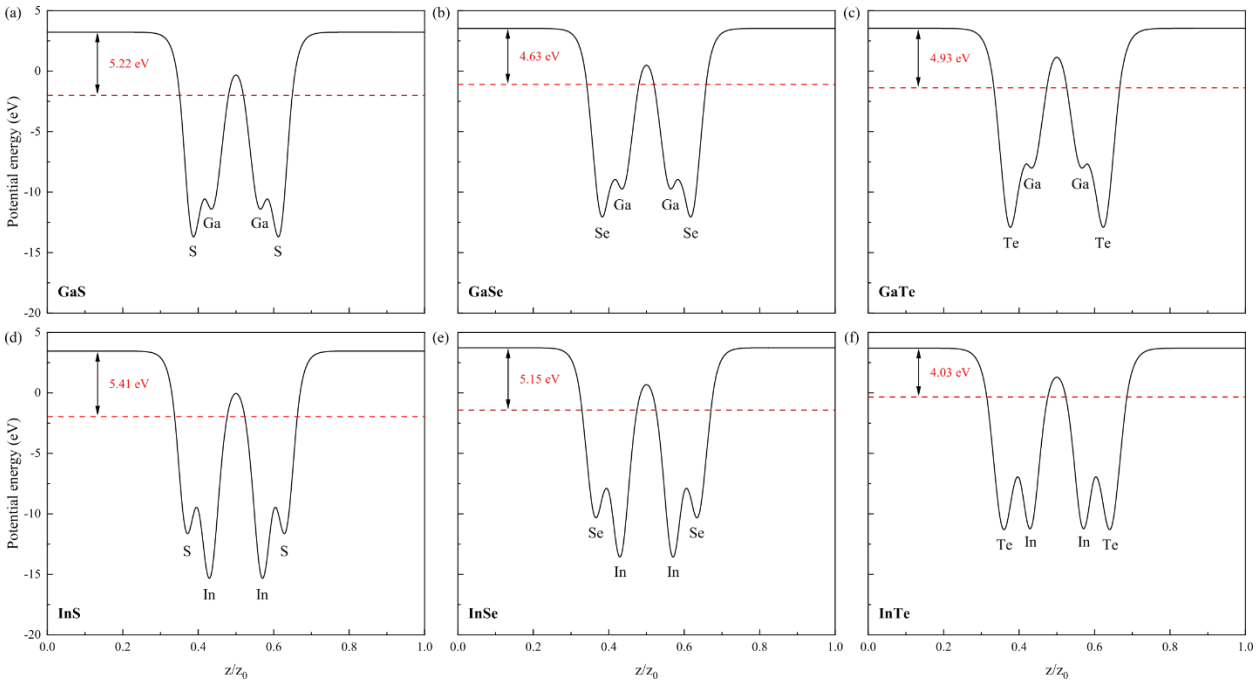

Figure S1. The plane-averaged electrostatic potential of monolayer (a) GaS, (b) GaSe, (c) GaTe, (d) InS, (e) InSe, and (f) InTe.

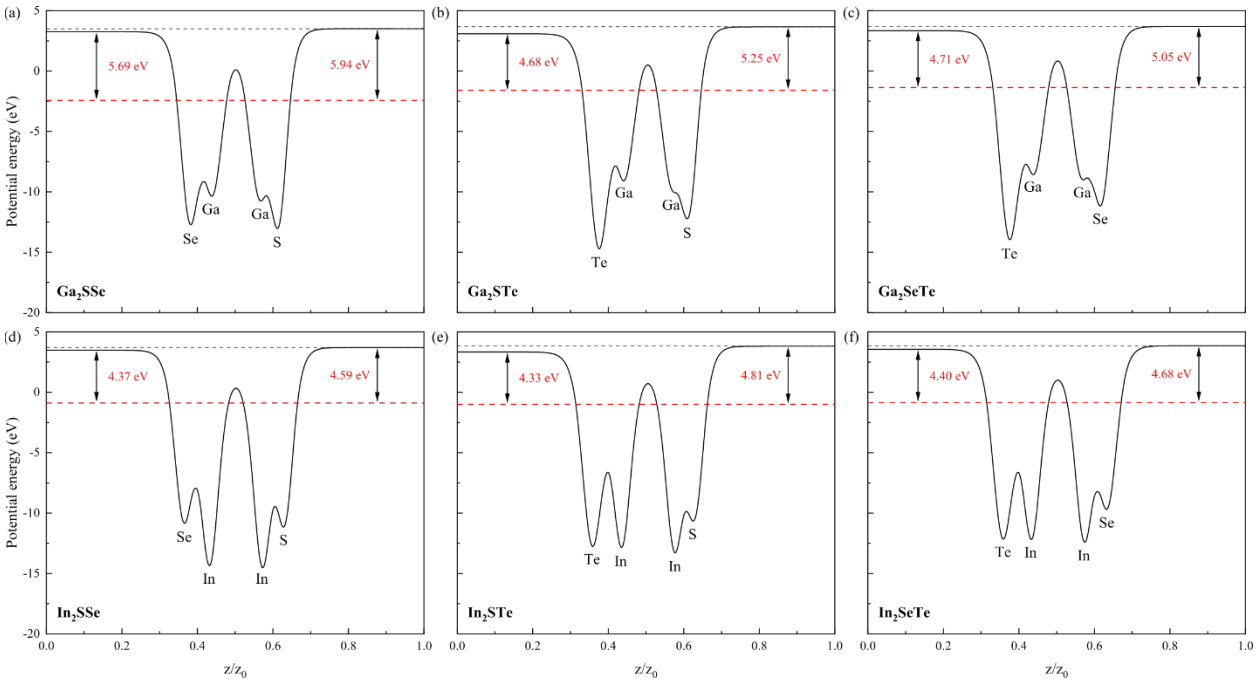

Figure S2. The plane-averaged electrostatic potential of monolayer (a) Ga_2SSe, (b) Ga_2STe, (c) Ga_2SeTe, (d) In_2SSe, (e) In_2STe, and (f) In_2SeTe.

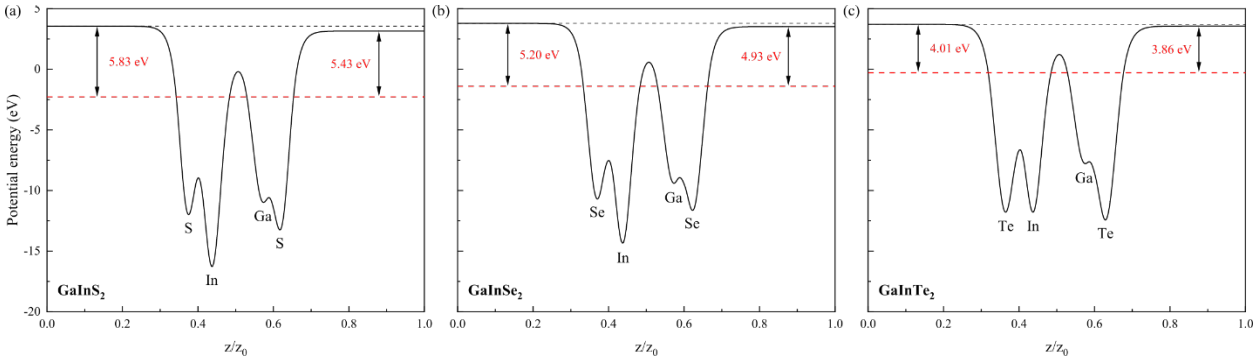

Figure S3. The plane-averaged electrostatic potential of monolayer (a) $GaInS_2$, (b) $GaInSe_2$, and (c) $GaInTe_2$.

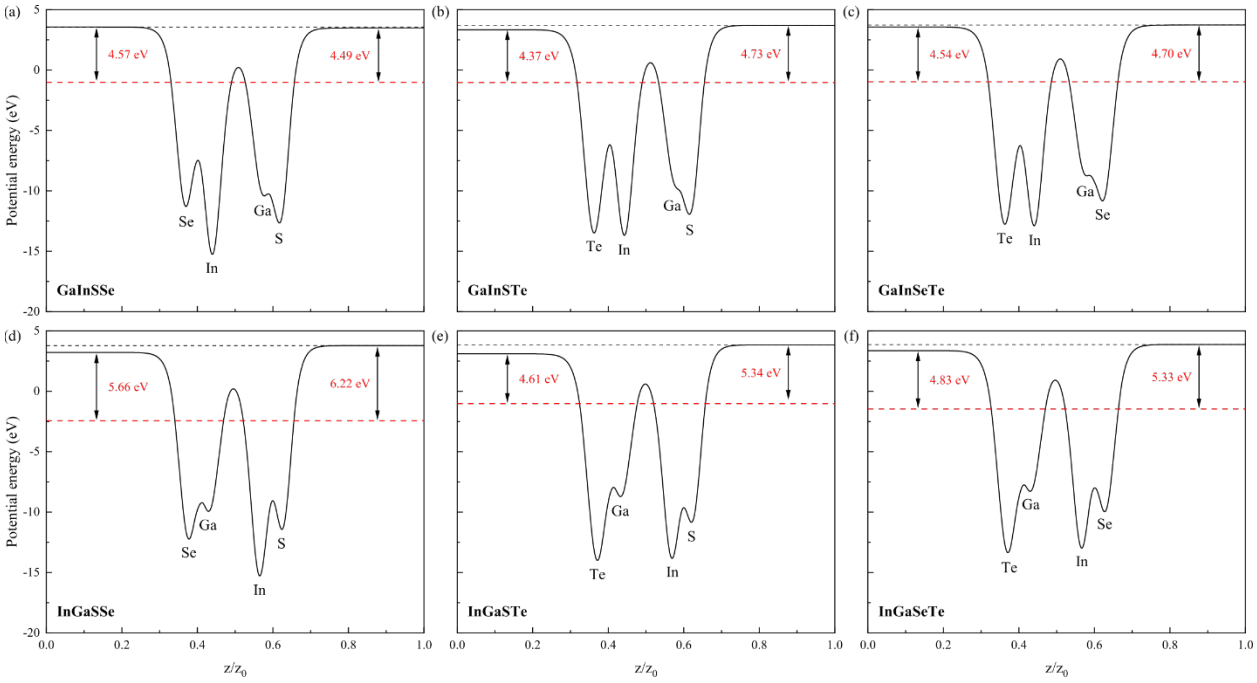

Figure S4. The plane-averaged electrostatic potential of monolayer (a) GaInSSe, (b) GaInSTe, (c) GaInSeTe, (d) InGaSSe, (e) InGaSTe, and (f) InGaSeTe.

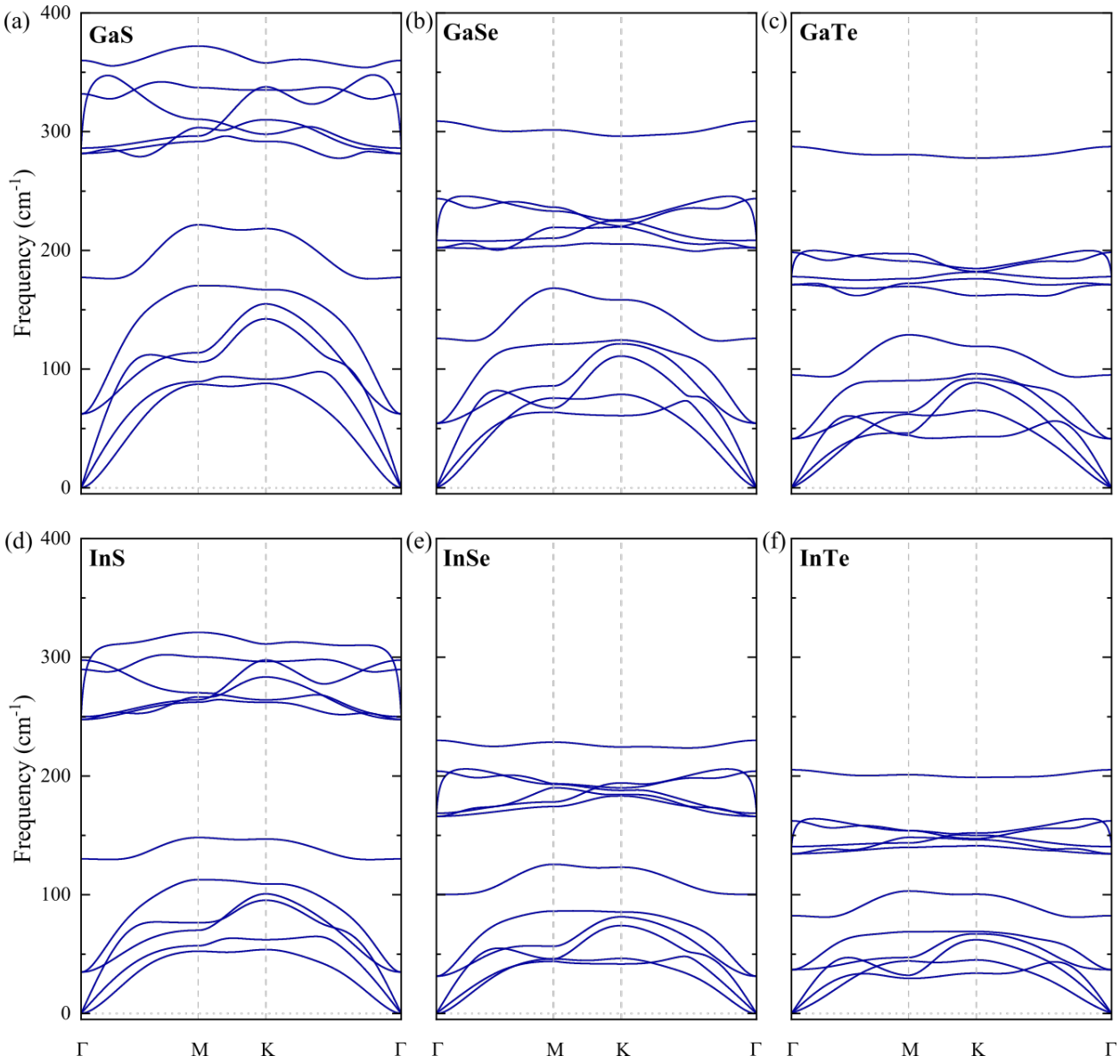

Figure S5. Phonon band diagrams of monolayer (a) GaS, (b) GaSe, (c) GaTe, (d) InS, (e) InSe, and (f) InTe.

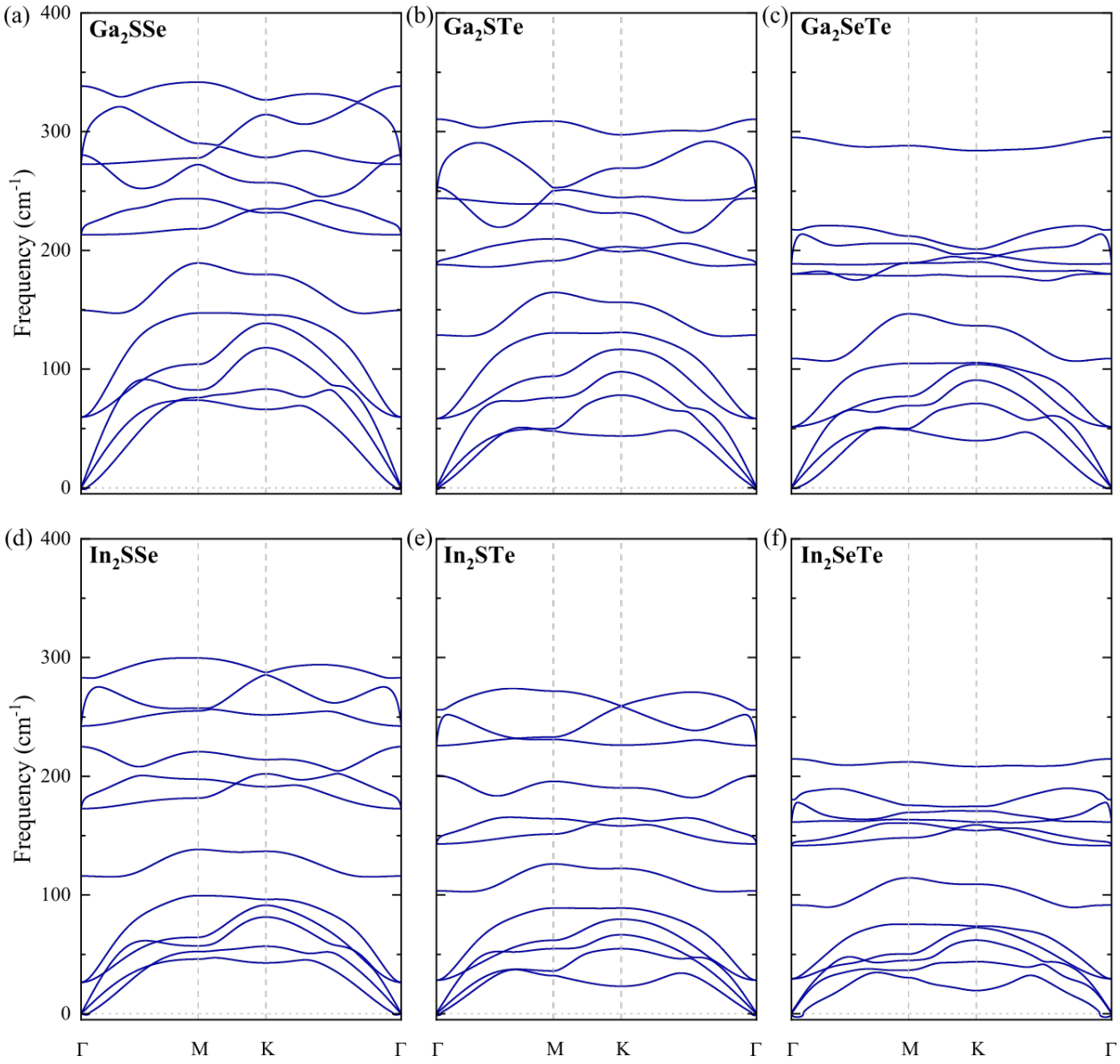

Figure S6. Phonon band diagrams of monolayer (a) Ga_2SSe, (b) Ga_2STe, (c) Ga_2SeTe, (d) In_2SSe, (e) In_2STe, and (f) In_2SeTe.

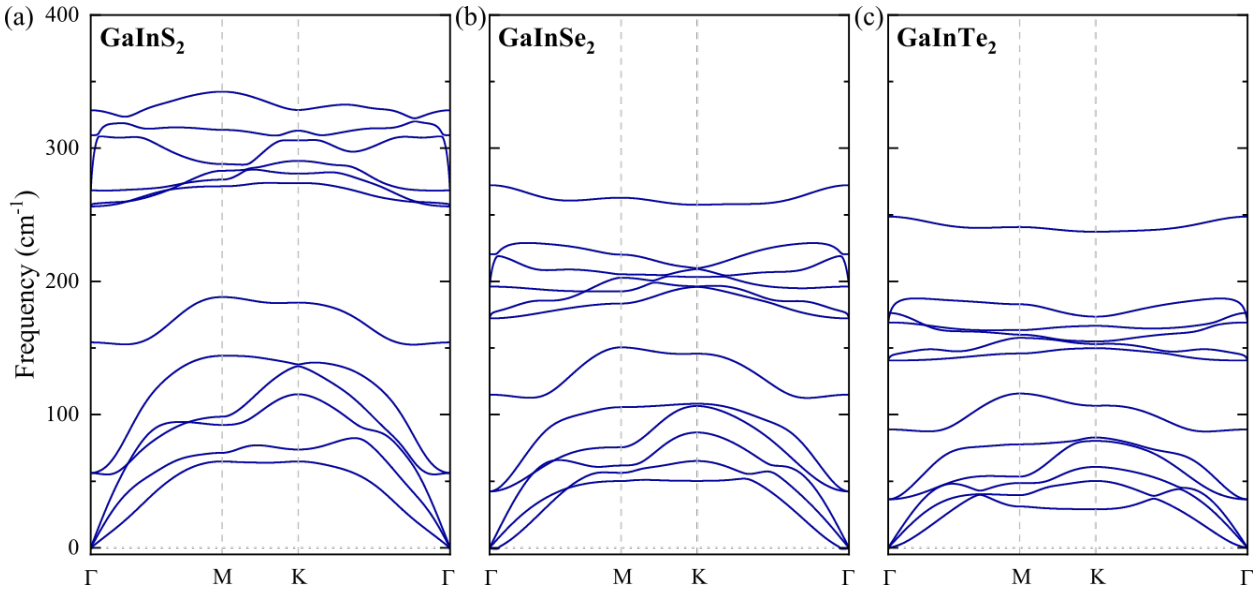

Figure S7. Phonon band diagrams of monolayer (a) $GaInS_2$, (b) $GaInSe_2$, and (c) $GaInTe_2$.

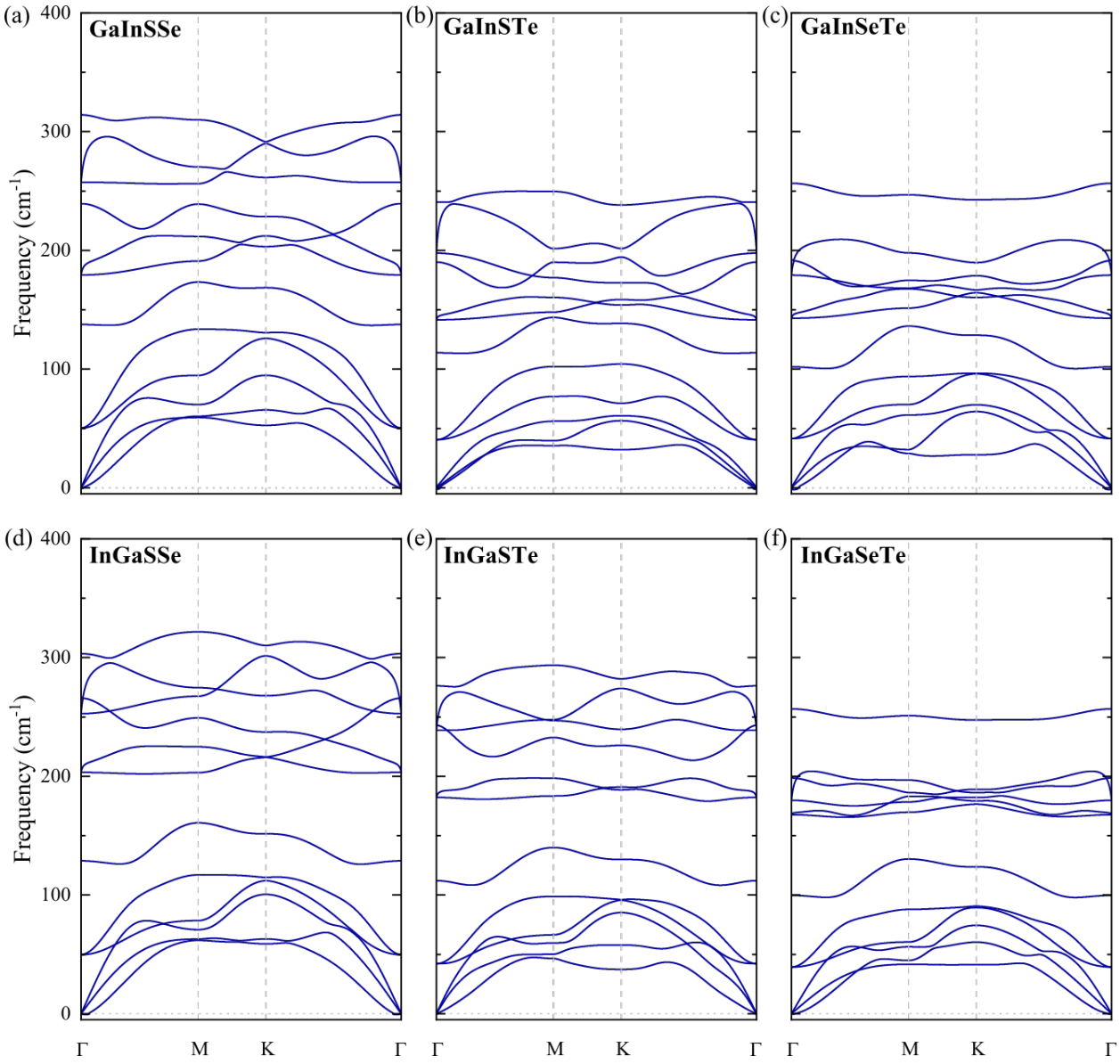

Figure S8. Phonon band diagrams of monolayer (a) GaInSSe, (b) GaInSTe, (c) GaInSeTe, (d) InGaSSe, (e) InGaSTe, and (f) InGaSeTe.

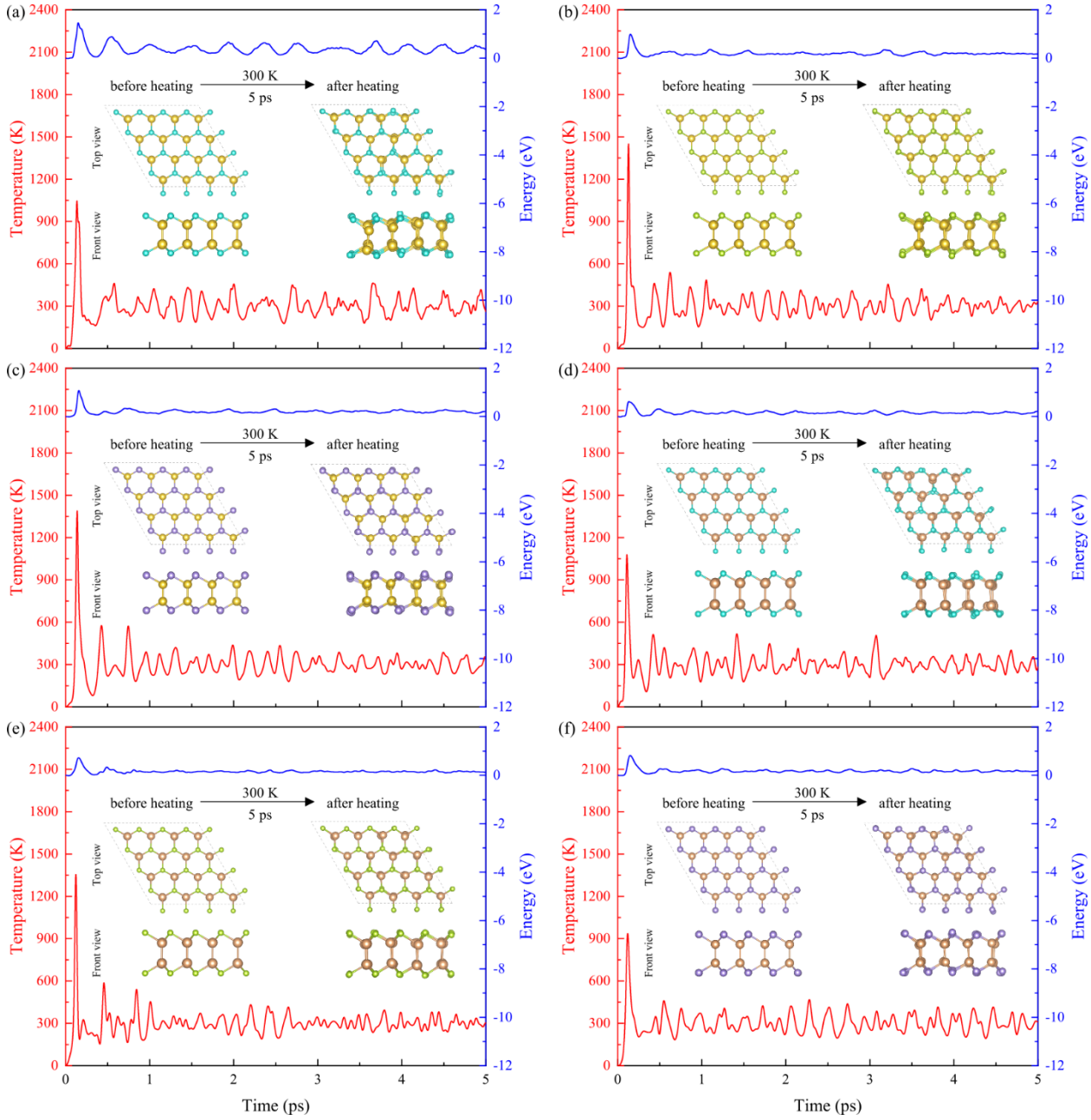

Figure S9. AIMD simulations of time-dependent temperature and relative energy fluctuations at room temperature of (a) GaS, (b) GaSe, (c) GaTe, (d) InS, (e) InSe, and (f) InTe monolayers. The insets are the snapshots of the atomic structures before and after heat treatment at 300 K within 5 ps.

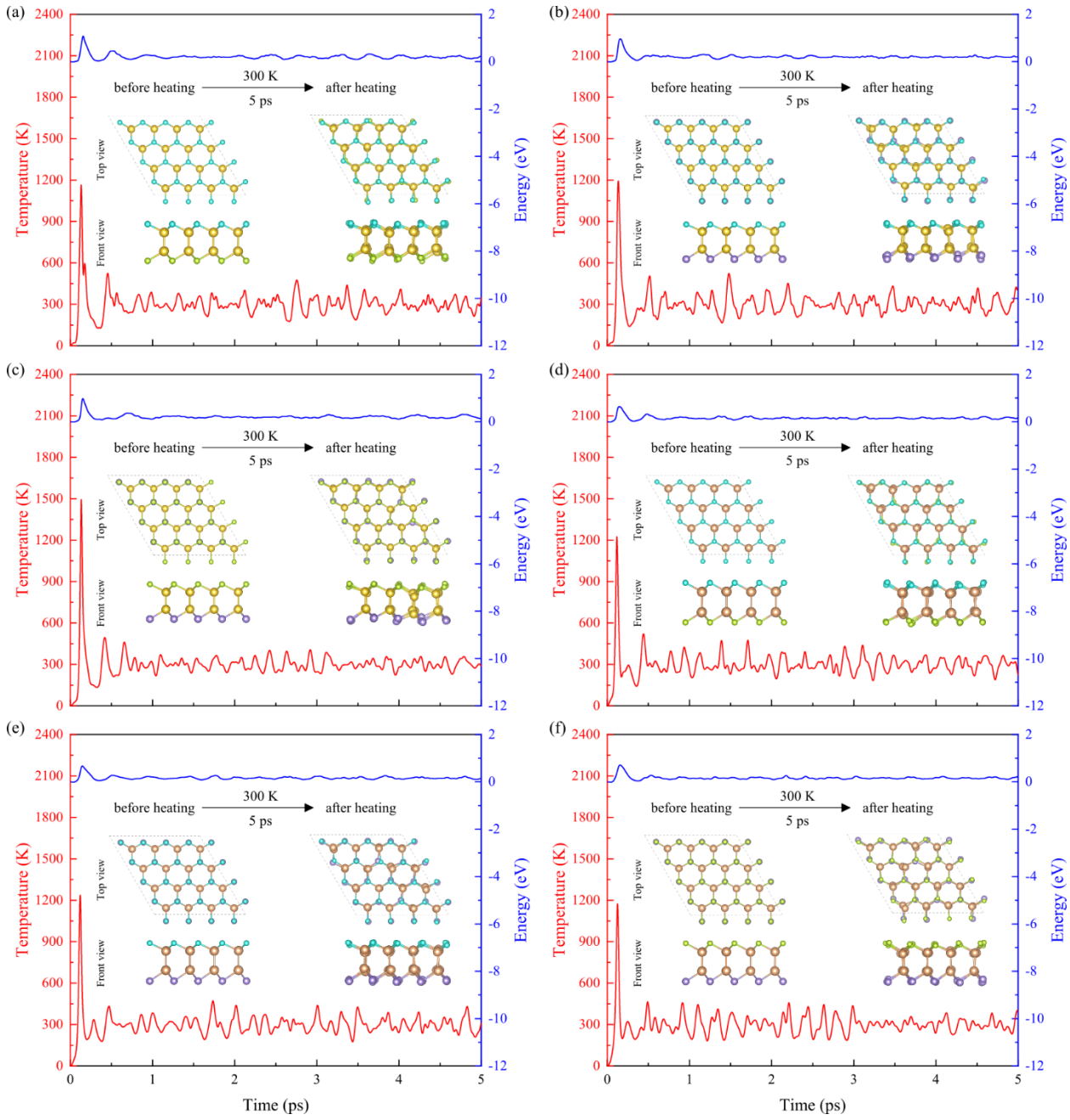

Figure S10. AIMD simulations of time-dependent temperature and relative energy fluctuations at room temperature of (a) Ga_2SSe, (b) Ga_2STe, (c) Ga_2SeTe, (d) In_2SSe, (e) In_2STe, and (f) In_2SeTe monolayers. The insets are the snapshots of the atomic structures before and after heat treatment at 300 K within 5 ps.

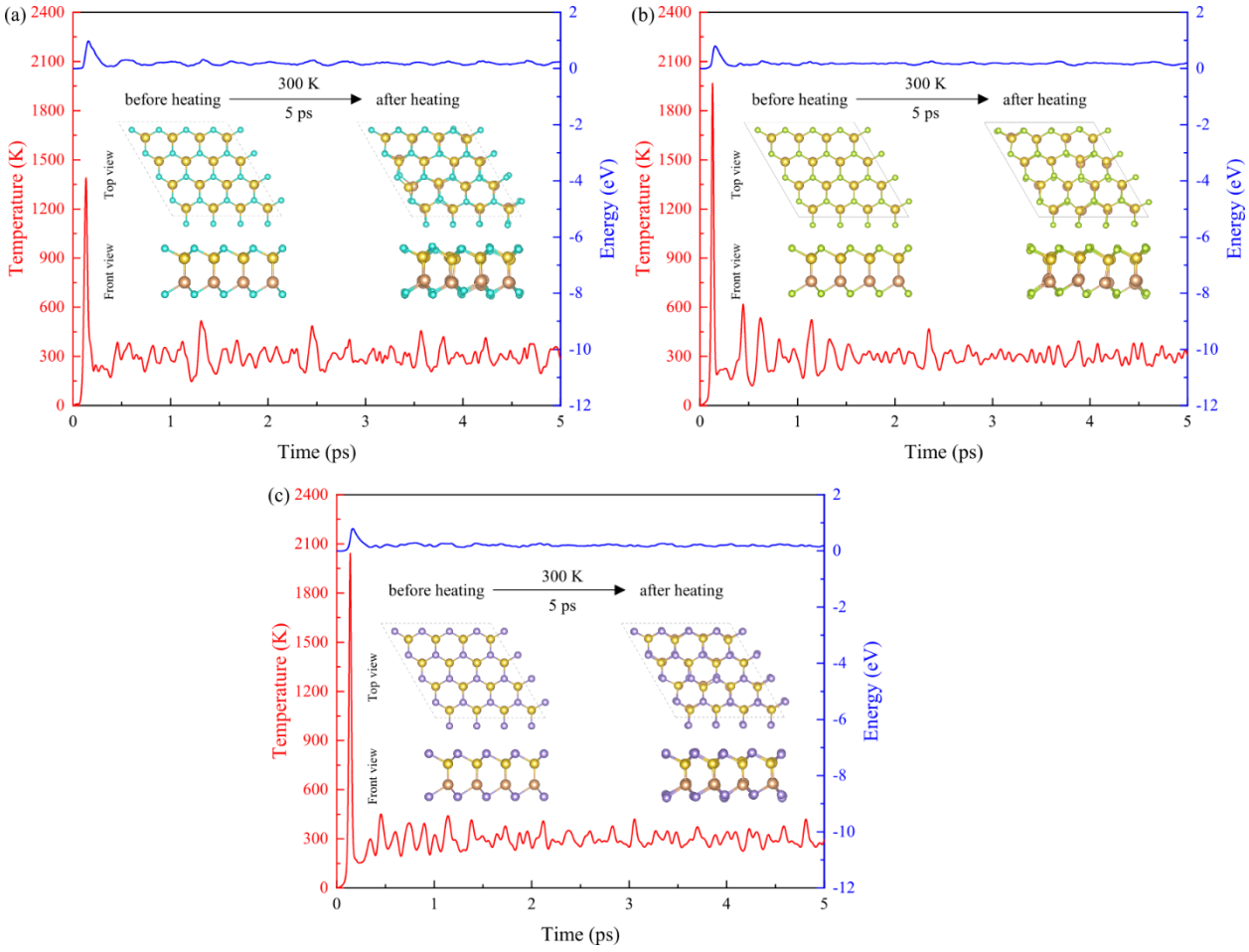

Figure S11. AIMD simulations of time-dependent temperature and relative energy fluctuations at room temperature of (a) $GaInS_2$, (b) $GaInSe_2$, and (c) $GaInTe_2$ monolayers. The insets are the snapshots of the atomic structures before and after heat treatment at 300 K within 5 ps.

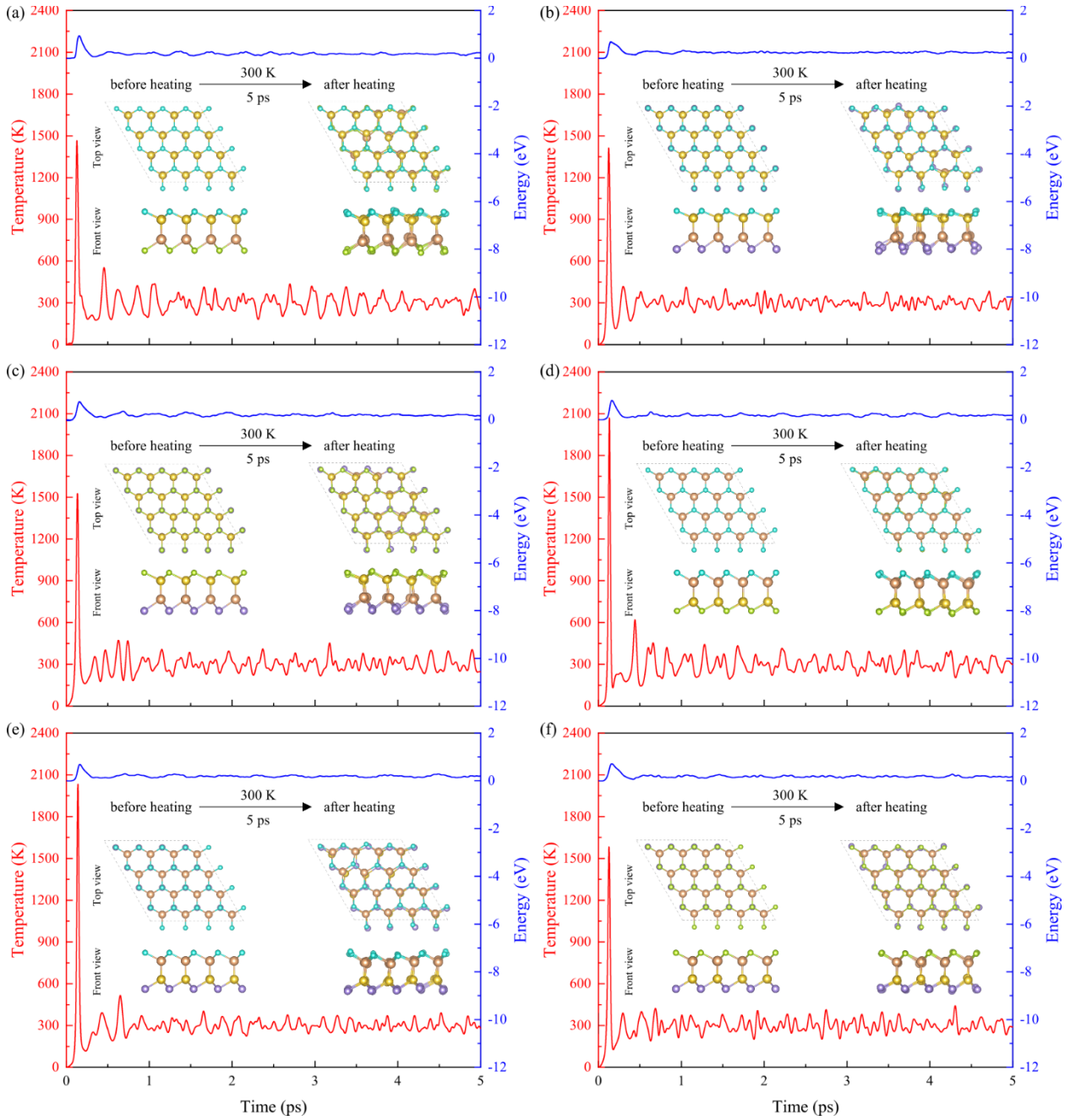

Figure S12. AIMD simulations of time-dependent temperature and relative energy fluctuations at room temperature of (a) GaInSSe, (b) GaInSTe, (c) GaInSeTe, (d) InGaSSe, (e) InGaSTe, and (f) InGaSeTe monolayers. The insets are the snapshots of the atomic structures before and after heat treatment at 300 K within 5 ps.

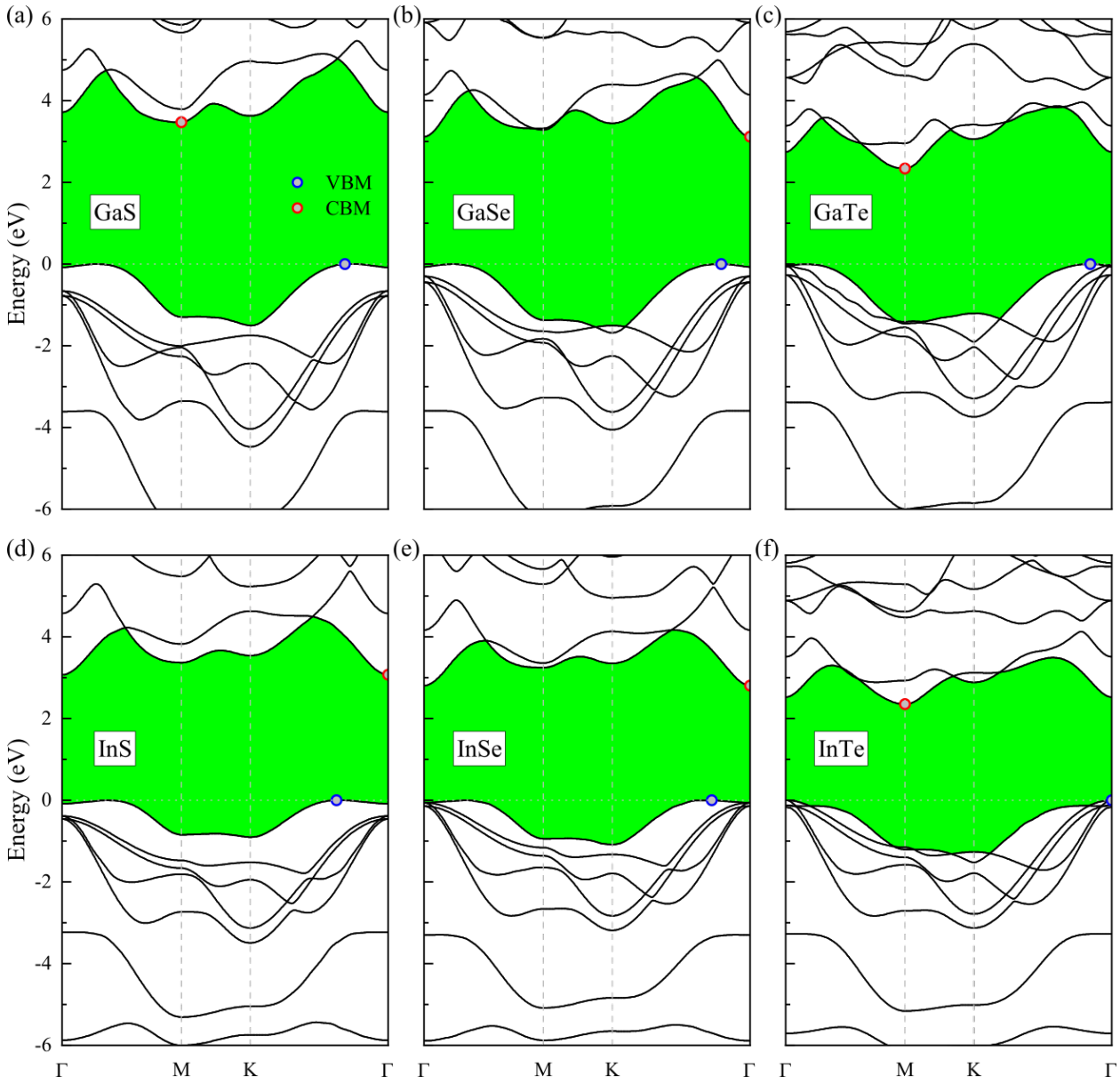

Figure S13. Band structures calculated using the HSE method for monolayer (a) GaS, (b) GaSe, (c) GaTe, (d) InS, (e) InSe, and (f) InTe. The valence band maximum is set to zero.

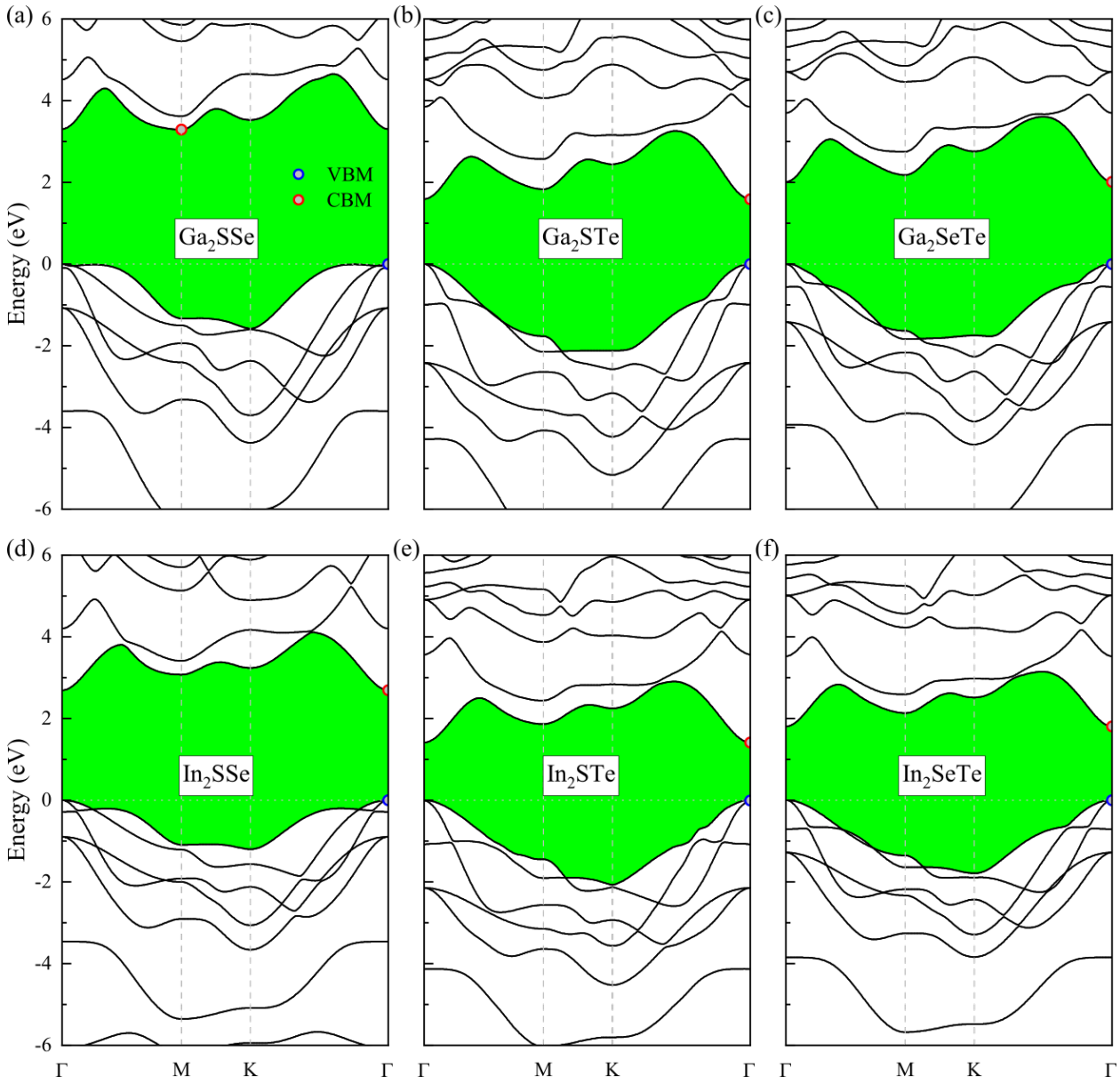

Figure S14. Band structures calculated using the HSE method for monolayer (a) Ga_2SSe, (b) Ga_2STe, (c) Ga_2SeTe, (d) In_2SSe, (e) In_2STe, and (f) In_2SeTe. The valence band maximum is set to zero.

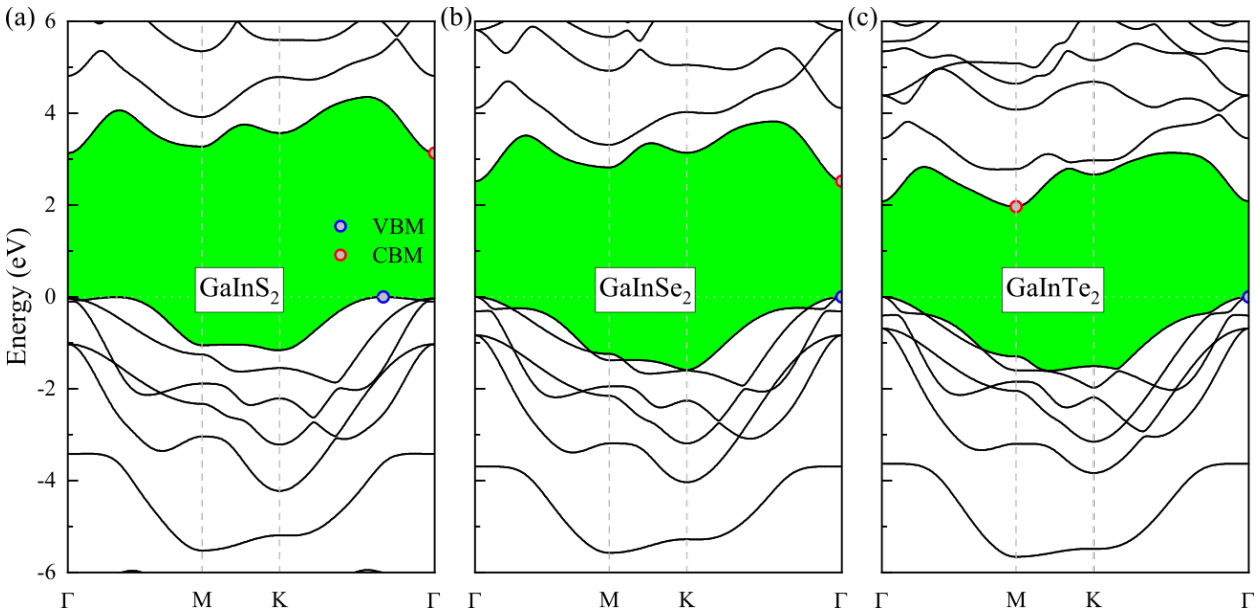

Figure S15. Band structures calculated using the HSE method for monolayer (a) $GaInS_2$, (b) $GaInSe_2$, and (c) $GaInTe_2$. The valence band maximum is set to zero.

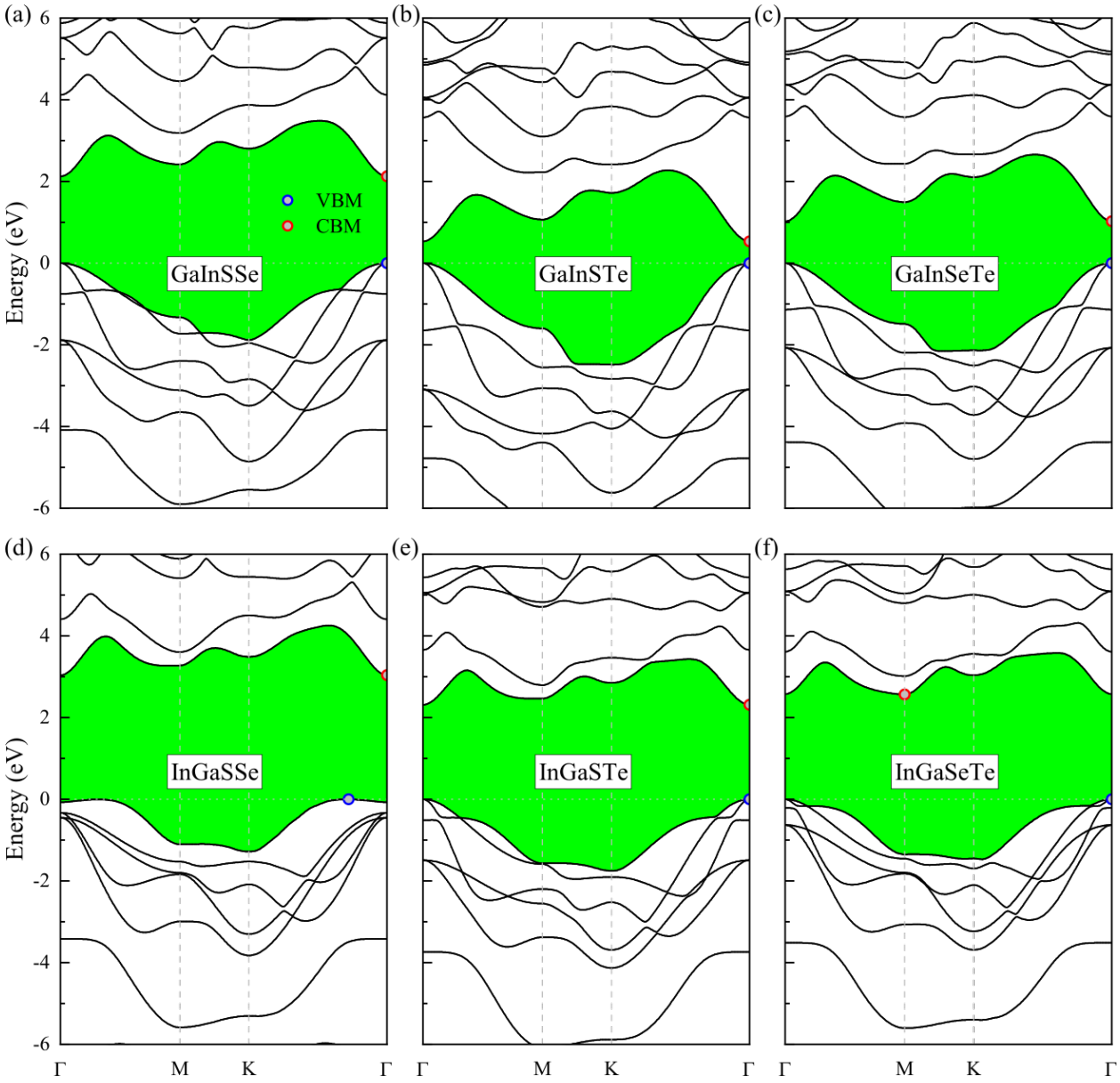

Figure S16. Band structures calculated using the HSE method for monolayer (a) GaInSSe, (b) GaInSTe, (c) GaInSeTe, (d) InGaSSe, (e) InGaSTe, and (f) InGaSeTe. The valence band maximum is set to zero.

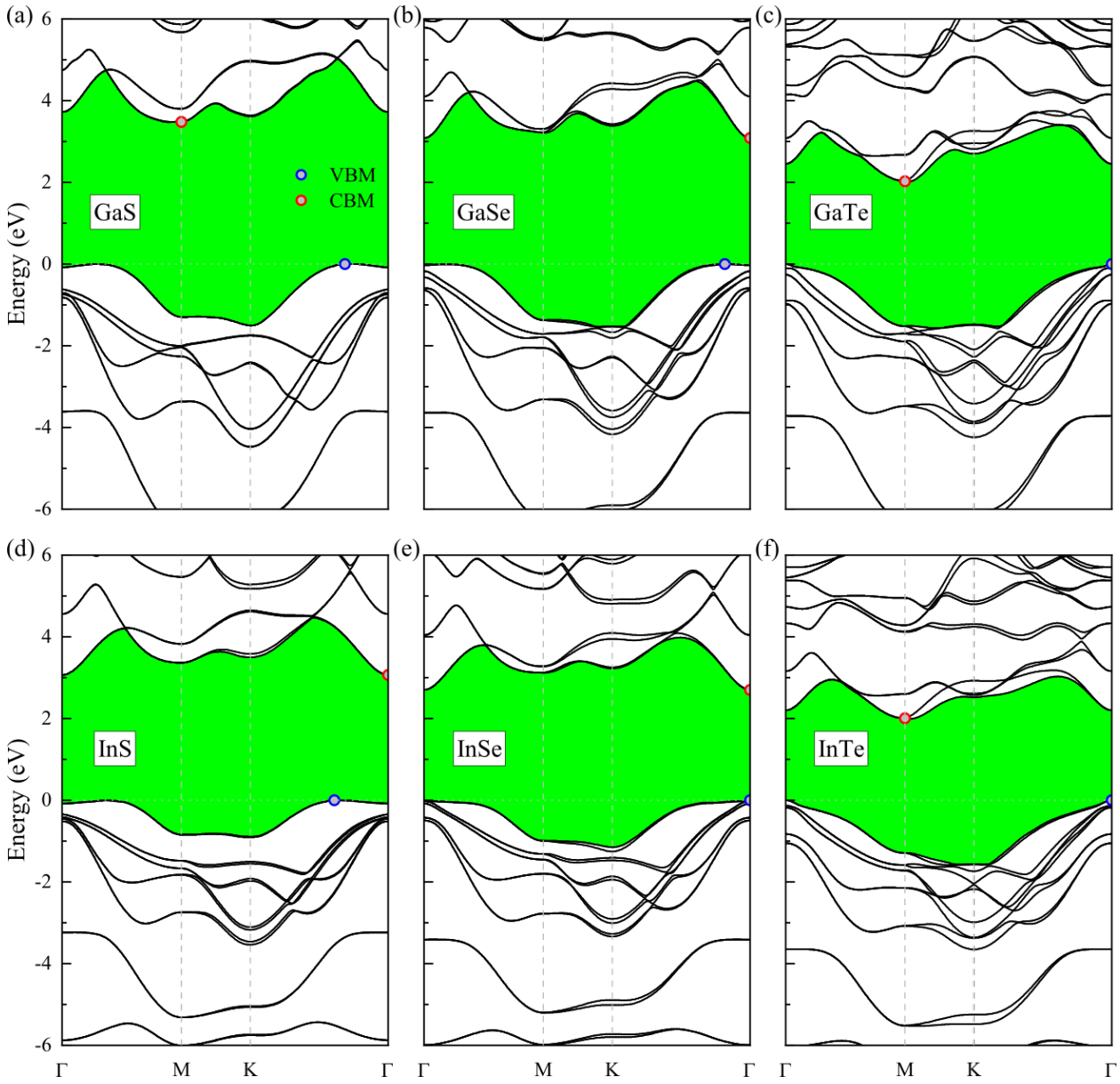

Figure S17. Band structures calculated using the HSE+SOC method for monolayer (a) GaS, (b) GaSe, (c) GaTe, (d) InS, (e) InSe, and (f) InTe. The valence band maximum is set to zero.

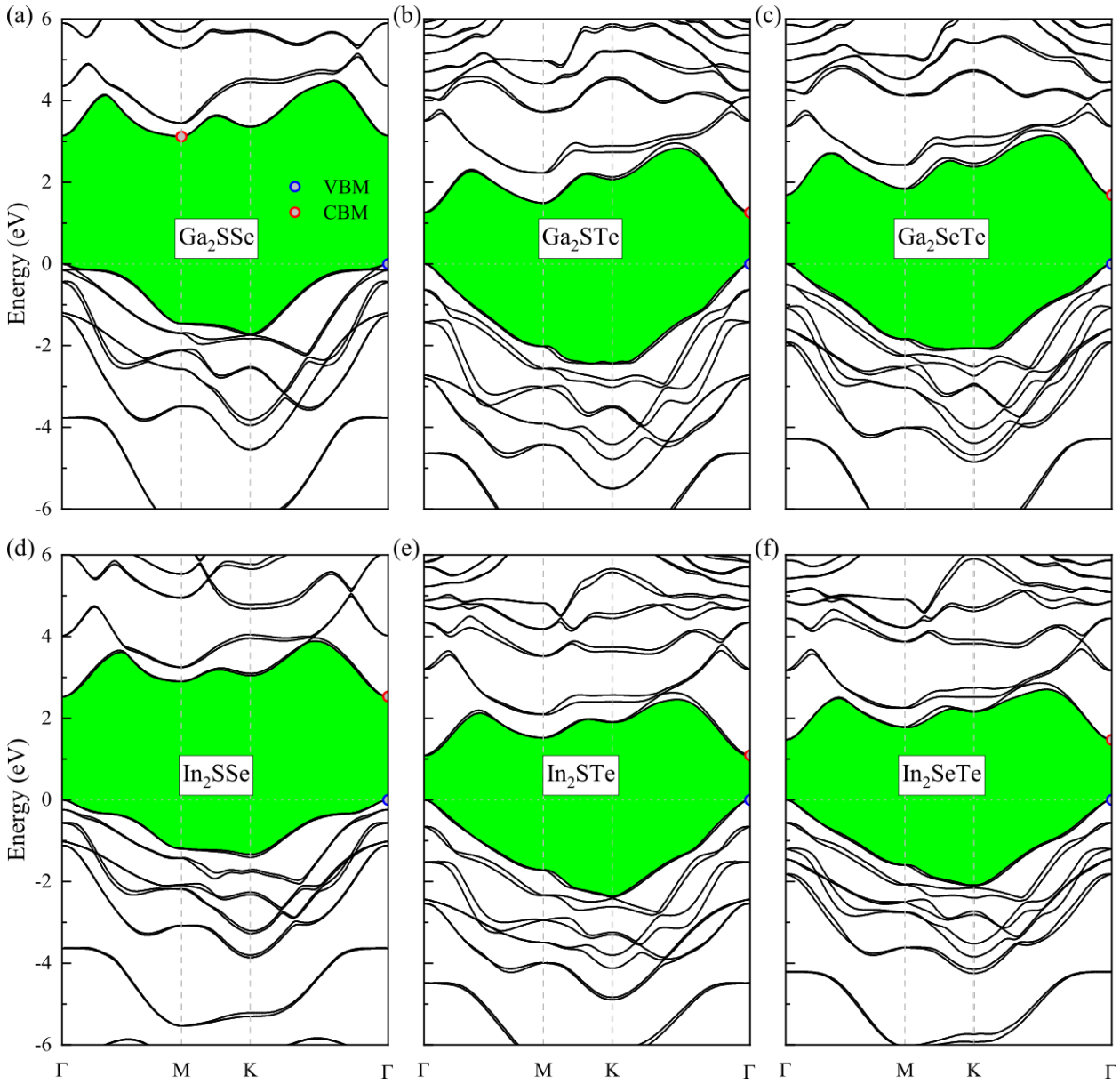

Figure S18. Band structures calculated using the HSE+SOC method for monolayer (a) Ga_2SSe, (b) Ga_2STe, (c) Ga_2SeTe, (d) In_2SSe, (e) In_2STe, and (f) In_2SeTe. The valence band maximum is set to zero.

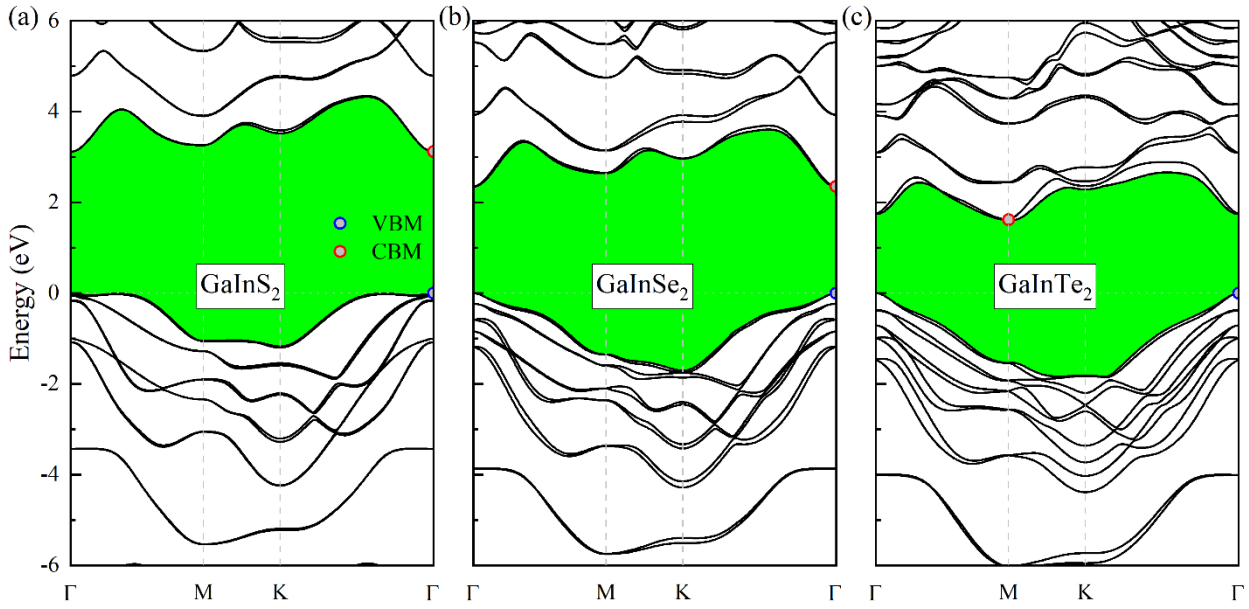

Figure S19. Band structures calculated using the HSE+SOC method for monolayer (a) $GaInS_2$, (b) $GaInSe_2$, and (c) $GaInTe_2$. The valence band maximum is set to zero.

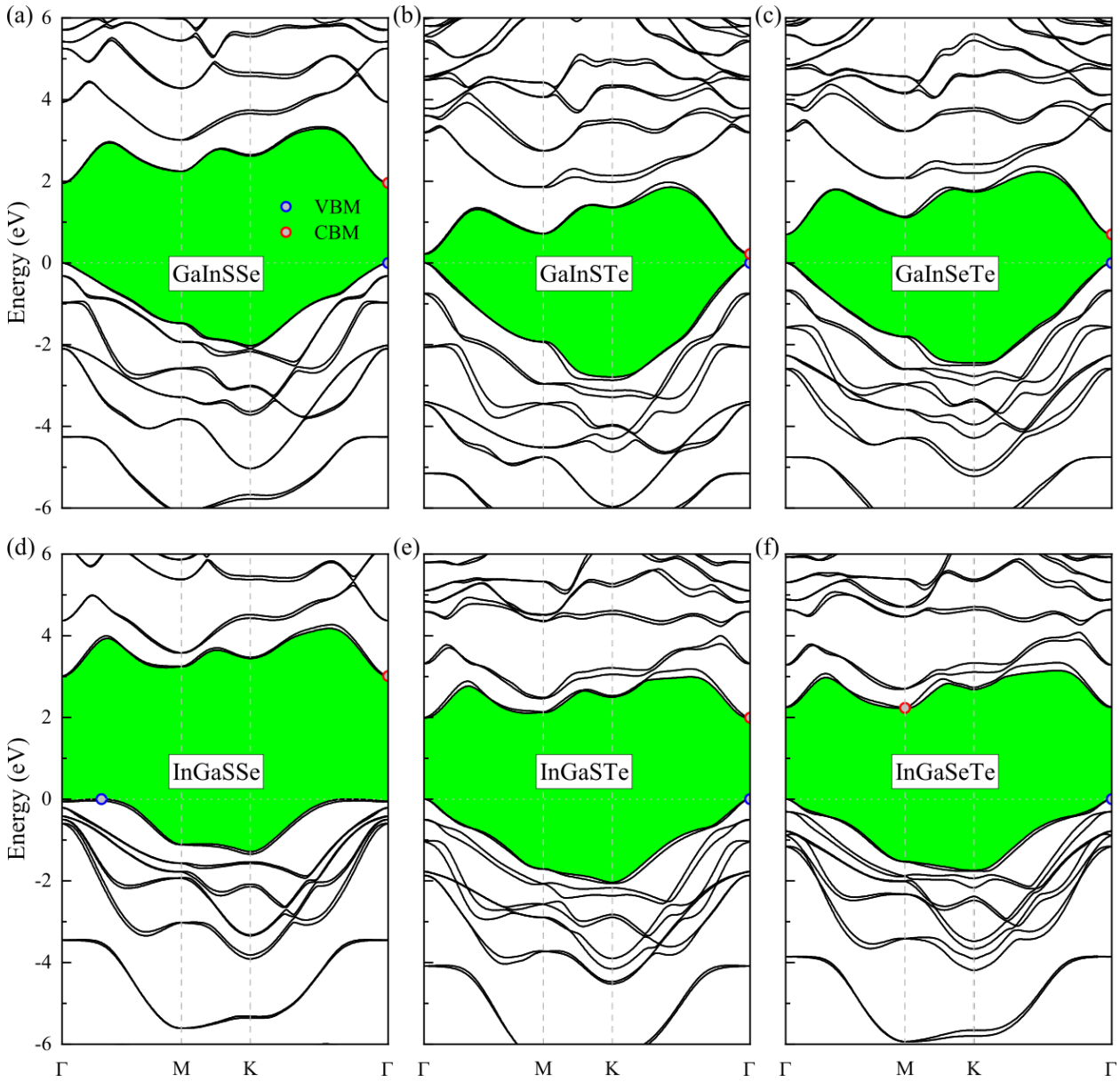

Figure S20. Band structures calculated using the HSE+SOC method for monolayer (a) GaInSSe, (b) GaInSTe, (c) GaInSeTe, (d) InGaSSe, (e) InGaSTe, and (f) InGaSeTe. The valence band maximum is set to zero.

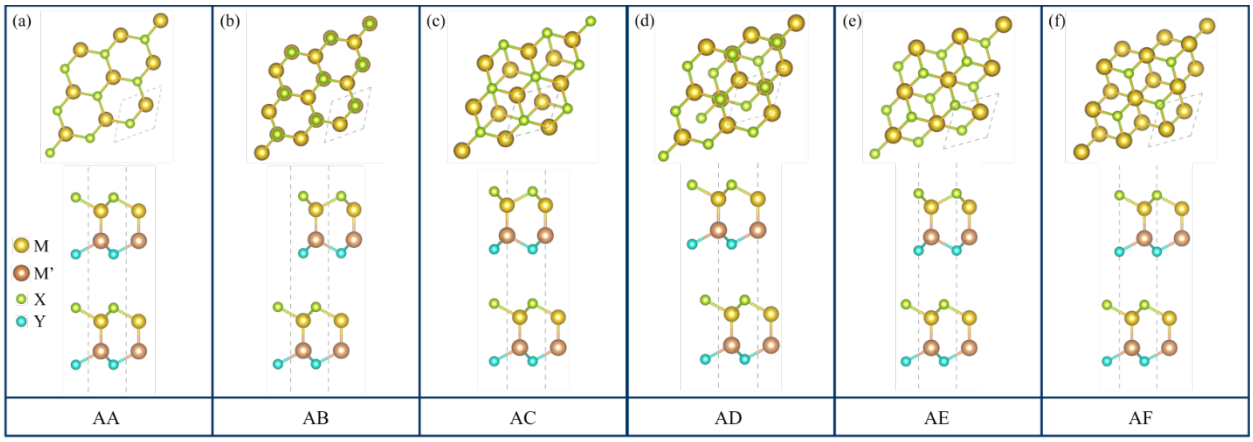

Figure S21. Top and side views of Janus group-III vdW heterostructure with six possible stacking configurations.

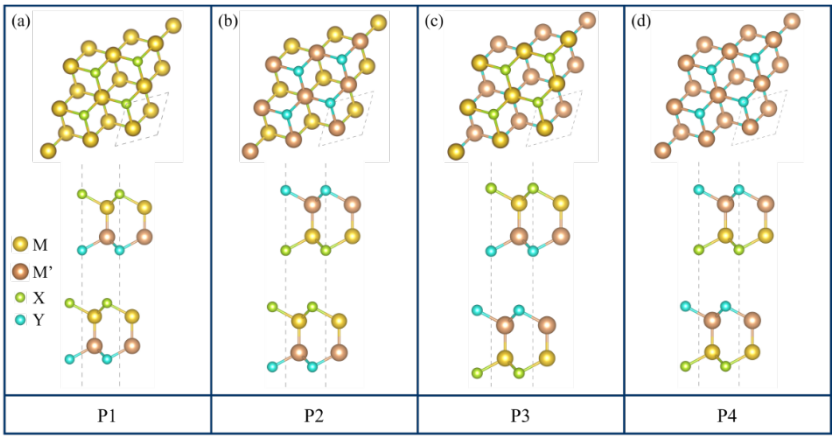

Figure S22. Top and side views of Janus group-III vdW heterostructure with four distinct interfacial patterns.

REFERENCES

[1] T. V. Vu, C. V. Nguyen, H. V. Phuc, A. Lavrentyev, O. Khyzhun, N. V. Hieu, M. Obeid, D. Rai, H. D. Tong and N. N. Hieu, Theoretical prediction of electronic, transport, optical, and thermoelectric properties of Janus monolayers In_2XO (X = S, Se, Te), Physical Review B, 2021, 103, 085422.

[2] S. Haastrup, M. Strange, M. Pandey, T. Deilmann, P. S. Schmidt, N. F. Hinsche, M. N. Gjerding, D. Torelli, P. M. Larsen, A. C. Riis-Jensen, and J. Gath, The Computational 2D Materials Database: high-throughput modeling and discovery of atomically thin crystals, 2D Materials, 2018, 5(4), 042002.

[3] M. N. Gjerding, A. Taghizadeh, A. Rasmussen, S. Ali, F. Bertoldo, T. Deilmann, N. R. Knøsgaard, M. Kruse, A. H. Larsen, S. Manti, and T. G. Pedersen, Recent progress of the computational 2D materials database (C2DB), 2D Materials, 2021, 8(4), 044002.